

www.acsaem.org Article

Carbon-Supported Platinum-Grafted Gold-Nickel Nanoclusters for Hydrogen Evolution Reaction

Lakshmi Kavalloor Murali, Kayalvizhi Anandhan, Subbiah Ravichandran, Edakkattuparambil Sidharth Shibu, and Jeyabharathi Chinnaiah*



Cite This: https://doi.org/10.1021/acsaem.5c01771



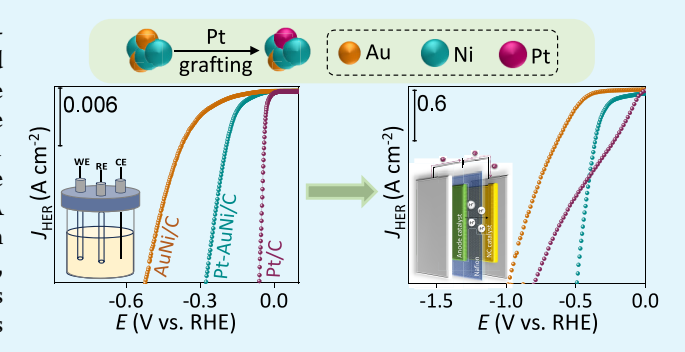
ACCESS I

III Metrics & More

Article Recommendations

sı Supporting Information

ABSTRACT: A carbon-supported platinum-grafted thiolate-protected precision AuNi nanocluster (NC) (Pt-AuNi/C) is studied for the hydrogen evolution reaction (HER) in acidic solution. The AuNi/C is doped with platinum through an electroless process. The HER performance is evaluated for AuNi/C and Pt-AuNi/C in a 0.1 M sulfuric acid solution. Typical HER behavior is noticed with the noticeable reduction in overpotential by ca. 208 mV_{RHE} @ 10 mA cm $^{-2}$ after platinum incorporation in the NCs. The HER curve on pristine NCs exhibits a contrasting steady-state limiting behavior, signaling a possible radial diffusion over the NCs. This result is expected for a random array-like arrangement of NCs, and this is witnessed as a changeover in steady-state limiting behavior to mass-



transport free characteristics with increased proton concentration. However, the steady-state limiting behavior is obscured by the carbon support. Further, the Pt-AuNi/C is tested in a zero-gap cell, where cathodic current density of $2.3~A~cm^{-2}$ was measured at the overpotential of $0.5~V_{RHE}$, which is much better than that of the benchmark Pt/C.

KEYWORDS: Precision AuNi nanocluster, Pt grafting, Radial proton diffusion, Hydrogen evolution reaction, Zero-gap cell

1. INTRODUCTION

Besides the transformational changes brought by the industrial revolution, the depletion of fossil fuels and environmental degradation emphasizes the importance of developing a sustainable energy source with zero carbon emission. ¹⁻³ The electrochemical water splitting technologies using renewable energy is a promising solution with the ease of access to water, ecofriendly combustion, and potential storage of clean energy, which, in turn, aids in the extensive implementation of renewable energy technologies. 4-6 The proton exchange membrane water electrolyzer (PEMWE) stands out among them for developing an energetically and environmentally sustainable future owing to its high efficiency, lower ohmic losses, fast response, safety, compact design, and gas purity. Nevertheless, large-scale water splitting remains limited by its reliance on expensive and less-abundant Pt-, Ru-, and Ir-based materials as electrocatalysts, that are implemented to improve the hydrogen evolution reaction (HER) and oxygen evolution reaction (OER) in PEMWE. 10-15 This necessitates the development of low-loading noble metal-based electrocatalysts. The integration of nanomaterials with water electrolysis technologies could help it to develop as a technologically and economically competitive option by increasing the active surface area, enhancing the mechanical strength, and improving catalytic activity with the use of a minimum amount of the catalyst. For unlocking the full potential of nano-

technology by bridging the stability and nanoparticle size trade-off, noble metal nanoclusters (NCs) can be considered as a promising class of materials due to their unique properties including ultrasmall size, larger surface-to-volume ratio, quantum confinement effect, and better stability. 16-24 Generally, pristine Au NCs are passivated by ligands, and their reactivity can be enhanced by atomic level modifications like foreign atom doping, core size tuning, ligand engineering, and ligand removal techniques. ^{21–25} Particularly, multimetal nanosystems have gained significant attention due to their tunable synergistic effect arising from the interaction between constituent elements. 26,27 For instance, doping Au NCs with foreign atoms such as Pt has been shown to enhance the reactivity that effectively reduces the Pt loading without compromising performance. 28,29 Similarly, AuNi bimetallic systems represent a versatile platform for electrocatalysis. While Au contributes to the exceptional stability of the nanoscale systems containing Au and Pt, Ni is an earthabundant metal and a cost effect option to lower the loading of

Received: June 10, 2025
Revised: September 2, 2025
Accepted: September 2, 2025



Au and Pt. Also, Ni contributes to escalate the reactivity through its ligand effect (electronic) with Pt and Au.^{30–33} Thus, the subnanometric integration of Au, Pt, and Ni in the NC system could modulate the electronic structure, enhance reactivity, and suppress the degradation of NCs. In this context, we have chosen AuNi bimetallic NCs as a promising platform for exploring next-generation electrocatalysts for the HER.

To tap the potentiality of Pt and AuNi NCs, we incorporated Pt into AuNi NCs and studied the HER performance using both conventional three-electrode and full-cell configurations. The Pt grafting on synthesized 2-phenylethanethiol (PET)-protected AuNi NCs was performed by an electroless method. The HER overpotential decreased by ca. 208 mV_{RHE} @ 10 mA cm $^{-2}$ after platinum incorporation in the AuNi/C in the half-cell study. Further, the carbon-supported Pt-grafted NCs (10% NCs onto Vulcan carbon) were used in a zero-gap cell with a Nafion 117 membrane for evaluating HER performance. The cathodic current density of 2.3 A cm $^{-2}$ was measured using 55 $\mu \rm g$ cm $^{-2}$ of Pt-AuNi at an overpotential of 0.5 $\rm V_{RHE}$, which is lower than that of the benchmark Pt/C.

2. EXPERIMENTAL SECTION

Reagents and Materials. All chemicals and solvents are of analytical grade and used without any further purification. Gold(III) chloride trihydrate (HAuCl₄·3H₂O), nickel(II) nitrate hexahydrate (Ni(NO₃)₂·6H₂O), 2-phenylethanethiol (PET), triethylamine, Vulcan carbon, Nafion ionomer (5 wt % in isopropyl alcohol), potassium hydroxide (KOH), sulfuric acid (H₂SO₄), isopropyl alcohol (IPA), methanol, acetone, dichloromethane (DCM), *n*-hexane, and acetonitrile (ACN) were purchased from Sigma-Aldrich. All of the electrochemical measurements were performed using ultrapure water (Milli-Q₄ 18.2 MΩ cm resistivity).

Synthesis of AuNi NCs. The AuNi-PET NCs was synthesized and purified with some modifications to the reported synthesis procedure. 34 In brief, Ni(NO $_3)_2\cdot 6H_2O$ (23.3 mg) and HAuCl $_4\cdot 3H_2O$ (20 mg) were dissolved in 2 mL of ACN in a 10 mL vial. The mixture was stirred vigorously for 20 min before the gradual addition of PET (36 μ L) followed by continued stirring for another 15 min. Triethylamine (36 μ L) was then introduced in a single dose, after which the reaction mixture was stirred for an additional 3 h. The supernatant containing the product was then collected by centrifugation and evaporated to dryness. To remove unreacted reactants and byproducts, the product was repeatedly washed with water and methanol. Separation of the product was carried out by preparative thin layer chromatography (PTLC) with 1:1 (v/v) DCM:n-hexane as the eluent. The top layer, corresponding to the required AuNi NCs, was extracted with DCM. The NCs were dried under vacuum and stored at 4 °C for further use.

Modifications of AuNi NCs and Electrode Preparation. In the initial set of experiments, the glassy carbon (GC) electrode was employed as the cathode, with 2 μ L of AuNi NCs (from 1 mg dissolved in 500 μ L of DCM) uniformly deposited via drop-casting. To incorporate Pt, the drop-casted AuNi NCs were immersed in a 1 mM H₂PtCl₆.xH₂O/water solution for 1 min. The modified GC electrode (with Pt-AuNi) was then meticulously rinsed with ultrapure water to remove any excess chloroplatinic acid, which was then used for electrochemical measurements in a three-electrode setup.

The NCs were incorporated into Vulcan carbon for extensive studies. To achieve this, 18 mg of Vulcan carbon was dispersed in 20 mL of DCM and sonicated for 30 min. Subsequently, 2 mg of AuNi NCs dissolved in DCM was added to the carbon suspension. The mixture was then subjected to magnetic stirring at room temperature for an additional 30 min. The 10% AuNi/C was separated from the solvent by centrifugation and dried under a vacuum. Afterward, 10 mg of the 10% AuNi/C was dispersed in 10 mL of 1 mM H₂PtCl₆xH₂O

solution prepared in ultrapure water. The suspension was stirred at room temperature for 30 min to facilitate Pt incorporation. The reaction mixture was then centrifuged to collect the product, followed by thorough washing with water for five times to remove any adsorbed $\rm H_2PtCl_6.xH_2O.$ Finally, AuNi/C and Pt-AuNi/C were dried under vacuum and stored at 4 °C for further characterizations and experimentation.

The electrochemical experiments were performed using a three-electrode setup, where the modified GC electrode acted as a working electrode with a Ag/AgCl (3 M KCl) electrode and Pt wire serving as the reference and counter electrodes, respectively. Prior to use, the 3 mm diameter GC electrode was polished with 0.05 μm alumina powder, rinsed thoroughly, and sonicated in Milli-Q water for 2 min. To prepare electrode material, 1 mg of the AuNi/C or Pt-AuNi/C or Pt/C was dispersed in a mixture of solvents containing 400 μL water, 70 μL IPA, and 30 μL Nafion, followed by 30 min of sonication to achieve a homogeneous ink. A 5 μL aliquot of this ink was then dropcast onto the cleaned GC electrode and allowed to dry before being used as the working electrode.

Instrumentation and Characterization. UV-vis absorption spectra were recorded by using a VARIAN Cary 500 Scan spectrometer. An electrospray ionization mass spectrum was collected from Waters SYNAPT XS high-definition mass spectrometer. Highresolution-transmission electron microscopy images, along with scanning transmission electron microscopy images, and elemental mapping were obtained utilizing a FEI Talos F200S transmission electron microscope operating at 200 kV. XPS spectra were collected using a Thermo Scientific ESCALAB 250Xi instrument with an XR6Microfocused Monochromator, utilizing Al K α X-rays. All electrochemical experiments (LSV, CV, and EIS) were executed using a SP-200 BioLogic workstation. All zero-gap cell tests were conducted at room temperature by using a high-current potentiostat (VMP3, BioLogic SAS). The RDE and stability tests were conducted by using Autolab with Nova 2.1 software. The electrochemical measurements were corrected for the uncompensated resistance. A compensation of 85% of the total iR drop was applied during measurements. The water contact angles of the modified membranes were measured using a goniometer (DataPhysics make).

Cataytic Activity Measurements. The HER performance was evaluated by using a three-electrode configuration with linear sweep voltammetry (LSV) in a deaerated 0.1 M $\rm H_2SO_4$ solution. Measurements were conducted in a potential range of 0.0 to -1.0 V vs Ag/AgCl at a scan rate of 5 mV s $^{-1}$.

Electrochemical activation was performed in 1 M KOH using a two-electrode system, where the modified GC electrode served as the working electrode, and the graphite rod functioned as the counter electrode. During electrochemical activation, a constant potential of -2.5 V was applied for 5 s to promote the dethiolation of the NCs. Following the activation, the GC electrode was rinsed gently with methanol and water before the electrocatalytic study.

RHE Potential Measurement and Reference Potential Correction. All experiments were conducted using a Ag/AgCl (3 M KCl) reference electrode, and the potentials were corrected to the RHE scale. The RHE potential was measured with a platinum rotating disc electrode (RDE) operating at 900 rpm in 0.1 M $\rm H_2SO_4$ by purging high-purity hydrogen.

EIS Measurements. Electrochemical impedance spectroscopy (EIS) measurements were conducted at different overpotentials using a conventional three electrode system in an inert atmosphere. A sinusoidal potential with an amplitude of 5 mV was applied over the DC potential, covering a frequency range of 100 kHz to 100 mHz with 10 points per decade. Nyquist plot fitting and analysis were then performed using ZSimp Win 3.21 software.

ECSA Measurements. The ECSA values of AuNi/C and Pt-AuNi/C were calculated from double layer capacitance ($C_{\rm dl}$). To determine the $C_{\rm dl}$, cyclic voltammograms are first recorded at various scan rates within the nonfaradaic potential window (0.0 to 0.1 V vs Ag/AgCl). These average capacitive current values are then plotted against their corresponding scan rates. Under conditions where only double-layer charging occurs, this plot yields a linear relationship and

the slope of the line corresponds to the $C_{\rm dl}$. Finally, the ECSA is calculated by dividing the obtained capacitance by the specific capacitance of a standard electrode material.

$$ECSA = \frac{C_{\rm dl}}{C_{\rm s}}$$

On the other hand, the Pt/C catalysts were initially activated by cycling between -0.2 to 1.2~V~vs Ag/AgCl in N_2 -purged $0.1~M~H_2SO_4$ solution at $100~mV~s^{-1}$, and ECSA was measured using CO-stripping technique. During the process, high-purity CO gas was purged through the solution for 9 min while maintaining the electrodes at -0.2~V to allow complete CO adsorption at active sites. After saturation, the electrolyte was bubbled with N_2 under the same conditions to remove excess/unadsorbed CO. Cyclic voltammetry was then performed in the potential window of $-0.2~to~0.9~V~at~50~mV~s^{-1}$. The total charge associated with the oxidative removal of adsorbed CO is integrated from the CO stripping peak, and the ECSA is calculated according to the equation:

$$ECSA = \frac{Q_c}{Q_c}$$

Fabrication of Membrane Electrode Assembly (MEA). The fabrication and testing of the MEA were conducted according to the reported procedures.⁵¹ The cathode catalyst ink was prepared by dispersing 5 mg of either 10% AuNi/C, 10% Pt-AuNi/C, or 10% Pt/ C in 100 μ L of a water-IPA-Nafion (8:1:1) solution. Similarly, the anode ink was formulated by mixing 50 mg of standard IrO2 in 100 μ L of the same solution mixture. Both inks underwent ultrasonication for 30 min, followed by magnetic stirring at 1000 rpm for an additional 30 min to ensure a uniform mixture. The cathode ink was brush coated on the carbon paper and incorporated onto the pretreated Nafion 117 membrane (3 cm × 3 cm). The opposite side of the membrane was then coated with IrO2 ink. Membrane electrode assemblies were integrated into the electrolyzer cell. The polytetrafluoroethylene gaskets were then used to achieve compression, and the cell was secured with four bolts and connected to an electrolyzer testing system. Deionized water was supplied to the anode at a flow rate of 5 mL min⁻¹.

3. RESULTS AND DISCUSSION

3.1. Synthesis of AuNi NCs and Electroless Pt Grafting. At first, the AuNi NCs were synthesized by the chemical reduction method using triethylamine as the reducing agent and 2-phenylethanethiol (PET) as the protecting ligand (Figure S1).³⁴ The electrospray ionization mass spectra (ESI-MS) of the purified NCs confirmed the formation and molecular composition of the NCs (Figure 1A), showing a major fraction (5.2:1) of Au₂Ni₃(PET)₈ along with Au₄Ni₂(PET)₈ that are denoted as AuNi NCs. The experimental isotopic patterns of both NCs match well with the theoretical patterns (inset in Figure 1A). The X-ray photoelectron spectroscopic (XPS) study of the NCs showed the presence of Au, Ni, and S in the NCs as evidenced from the Survey spectrum (Figure S2). Au and Ni are in the Au⁺ (Figure 1B) and Ni²⁺ (Figure 1C) states with the binding energy values of 84.74 eV (Au $4f_{7/2}$) and 88.44 eV (Au $4f_{5/2}$), and 855.80 eV (Ni $2p_{3/2}$) and 873.28 eV (Ni $2p_{1/2}$).

To incorporate Pt in the NCs, the glassy carbon (GC) electrode coated with NCs was dipped in a H₂PtCl₆ solution that resulted in the electroless incorporation of Pt(II) in the NCs (Pt-AuNi). This is due to the reduction of Pt(IV) by the size-dependent reactivity of the NCs.^{35,36} The absorption spectra of the Pt-AuNi NCs showed similar absorption peaks at 320, 340, 428, and 540 nm as in the pristine NCs, revealing that the core structure remained intact (Figure 1D).³⁷ The voltammetric behavior of the AuNi and Pt-AuNi NCs showed

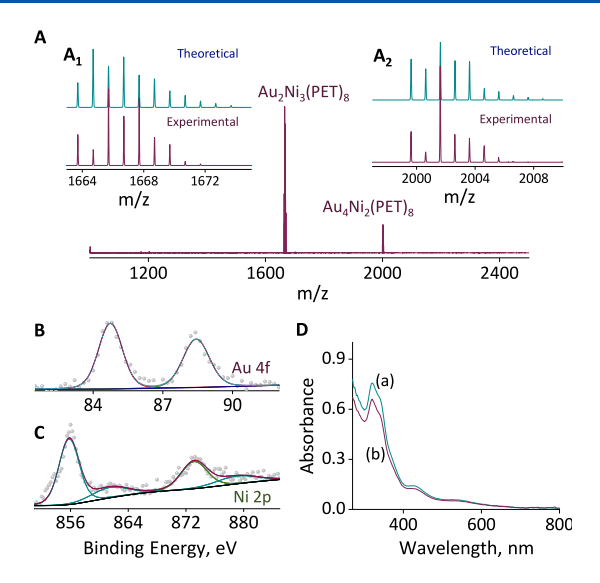


Figure 1. (A) ESI-MS spectra of the synthesized NCs showing the experimental and theoretical isotopic patterns of (A_1) $Au_2Ni_3(PET)_8$ and (A_2) $Au_4Ni_2(PET)_8$. (B) XPS spectra corresponding to (B) Au 4f and (C) Ni 2p in the pristine AuNi NCs. (D) UV—vis absorption spectra of the NCs (a) before and (b) after electroless Pt grafting.

primarily capacitive characteristics (Figure S3). Moreover, the increase in the cathodic current density at a negative of 0.05 V vs RHE indicates the promotion of HER by Pt-grafted NCs. Further to monitor Pt incorporation, cyclic voltammogram (CV) was performed in an inert atmosphere after exposure to carbon monoxide (CO). The absence of the CO-stripping peak reaffirms that the Pt is in the Pt(II) oxidation state (Figure S4).

3.2. Evaluation of HER Performance of Pristine NCs. The effect of Pt grafting on the water splitting reaction was then monitored. The HER polarization curves of the AuNi and Pt-AuNi modified GC electrode coated with 57 μ g cm⁻² of NCs revealed a unique quasi-steady state behavior followed by a steep increase in HER current at higher overpotentials in 0.1 M $\rm H_2SO_4$ recorded at 5 mV s⁻¹ (Figure 2A). A similar steady-state behavior was reported prior to the main HER process on the Au NCs, which was supposed to be due to the steady-state desorption of hydrogen.³⁸ However, the reason for the reduction of proton at a low overpotential than the main HER process was not provided. Since steady state can be achieved due to confinement of fixed diffusion layer thickness, we assumed a possible random-array like behavior.

If the mass transport is enhanced, the steady-state current would enhance, or mass-transport free current would be flowing. Thus, we enhanced the concentration of the H₂SO₄ from 0.1 to 0.5 M, where a quasi-steady state behavior was witnessed. With further increase in proton concentration to 1.0 M H₂SO₄, a significant increase in HER current was achieved at low overpotentials, and the steady-state behavior was almost lost (Figure 2B). Typically, steady-state limiting behavior is achieved under hydrodynamic conditions and on the surface of ultramicroelectrodes. For HER, mass-transport limited proton reduction has been shown to occur in mildly acidic solutions prior to the water reduction under hydrodynamic conditions, where mass transport can be enhanced by increasing the rotation rate (thinner Nernst diffusion layer thickness). 39,40 To further understand the quasi-steady state HER behavior of Pt-AuNi NCs, HER polarization curves were recorded in 0.1 M

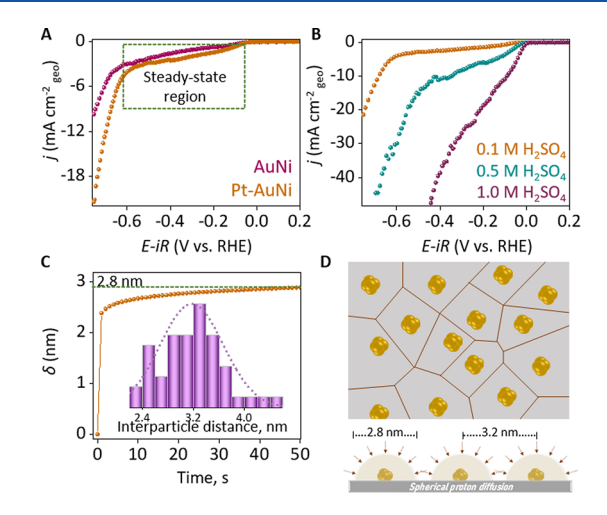


Figure 2. (A) HER polarization curve of pristine AuNi and Pt-AuNi NCs in 0.1 M H_2SO_4 at 5 mV s⁻¹. (B) HER polarization curves of Pt-AuNi NCs at different molar concentrations of H_2SO_4 at 5 mV s⁻¹. (C) Theoretical curve of diffusion layer thickness over the NCs with the core size of 0.5 nm. The inset shows the histogram of interparticle distance as measured from Figure 3D. (D₁, D₂) Schematic showing the random NCs array and NC-confined diffusion fields.

 $\rm H_2SO_4$ by using a rotating disk electrode (RDE) at varying rotation rates (Figure S5). As the rotation rate increased from 100 to 2500 rpm, the HER current density increased that also exhibited the quasi-steady state behavior. At 100 rpm, the quasi-steady state is prominent. As the rotation rate is increased, the quasi-steady state behavior was suppressed since the flux of the protons to the electrode increased. The effect of increasing $\rm H_2SO_4$ concentration and the RDE results suggest that mass transport is the limiting factor. This is possible due to the arrangement of the NCs as a random array of tiny electrodes, ^{41–44} driven by their intrinsic self-assembling characteristics. To support this idea, we calculated the diffusion layer thickness (δ) for the array of micro/nano electrode with respect to time using the following equation.

$$\delta = \frac{W}{\frac{1}{\sqrt{\pi\theta} + 0.97 - 1.10 \exp\left[\frac{-9.90}{\ln(12.37\theta)}\right]}}$$

where $\theta = \frac{Dt}{w^2}$ and D is the diffusion coefficient. The value for W (width of the nanoelectrode) was measured from the highresolution transmission electron microscopy (HRTEM) image of the Pt-AuNi/C as 0.5 nm (size of the NC). From Figure 2D, the diffusion layer thickness was calculated as 2.8 nm on the surface of 0.5 nm NCs. On the other hand, the histogram (inset of Figure 2C) showed the average interparticle distance of the NCs as measured from Figure 3D. Assuming that the interparticle distance is larger in pristine NCs, the calculated diffusion layer thickness suggests the confinement of diffusion field at the NCs surface and facilitates the radial diffusion of proton resulting in mass-transport limited proton reduction. This is viewed as a consequence of the random arrangement of NCs, where partial overlap of diffusion field (mixed diffusional field) is expected after t > 0 that would result in quasi-steady state limiting behavior. As the overpotential increases, the quasi-steady state behavior is changed to a steep HER response due to complete overlap of diffusion fields resulting in planar diffusion field. However, the origin of a quasi-steady state in highly acidic solution is puzzling, where mass transport of proton is not a problem. Based on these observations, we suggest the extent of hydrophilic surface sites and hydrophobic ligands of the NCs that would play a role in controlling the wettability⁴⁶ at the monatomic surface sites and aid the H₃O⁺ transport toward the active sites.⁴⁷ The contact angle data (vide infra) support these arguments, where the AuNi/C is relatively more hydrophobic than the Pt-AuNi/C.

3.3. Electrocatalytic HER Performance of Pt-AuNi/C in Half-Cell. The NCs were then introduced into the Vulcan carbon support (10 wt % AuNi/C). The AuNi/C was then stirred with a 1 mM H_2PtCl_6 solution for 30 min to incorporate the Pt into the NCs (Pt-AuNi/C). During the comparison of XPS spectra of Au 4f, we observed a change in peak position for Pt-AuNi/C [84.59 eV (Au $4f_{7/2}$) and 88.28 eV (Au $4f_{5/2}$); Figure $3A_1$] from AuNi/C [84.85 eV (Au $4f_{7/2}$) and 88.54 eV (Au $4f_{5/2}$); Figure $3A_2$]. The peak shift of 0.26

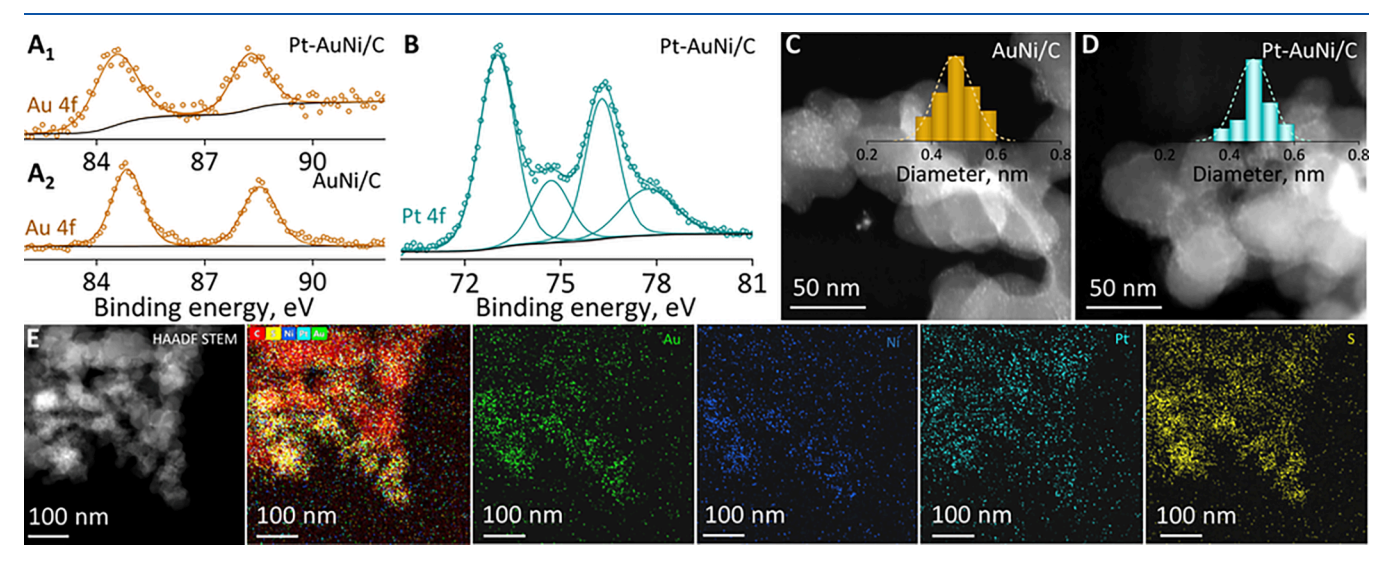


Figure 3. XPS spectra corresponding to (A) Au 4f of (A₁) Pt-AuNi/C, (A₂) AuNi/C, and (B) Pt 4f of Pt-AuNi/C. HAADF-STEM image of (C) AuNi/C and (D) Pt-AuNi/C along with the size distribution histograms. (E) Elemental maps for Pt-AuNi/C (elements are denoted in each image).

ACS Applied Energy Materials

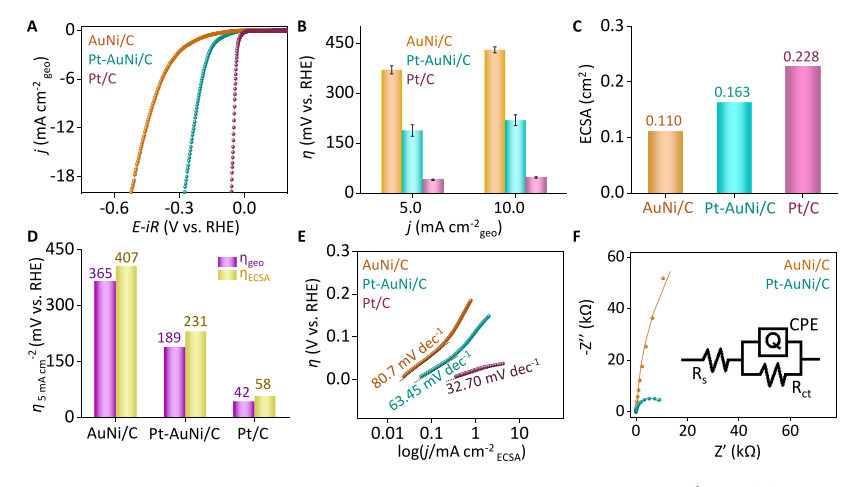


Figure 4. (A) HER polarization curves of AuNi/C, Pt-AuNi/C, and Pt/C in 0.1 M $\rm H_2SO_4$ at 5 mV s⁻¹ and (B) comparison of HER overpotentials at different current densities. (C) Comparison of calculated ECSA of the electrocatalysts and (D) comparison of overpotentials of both geometrical and ECSA-normalized plots at 5 mA cm⁻². (E) iR-corrected Tafel plots from ECSA-normalized curves. (F) Comparison of Nyquist plots of AuNi/C and Pt-AuNi/C at an overpotential of -0.35 V vs Ag/AgCl along with the corresponding Randles equivalent circuit (R_s - solution resistance; R_{ct} - charge transfer resistance; CPE - constant phase element).

eV to a lower BE indicates a decrease in the electropositive character of Au 4f. On the other hand, as shown in Figure 3B, new Pt 4f peaks appeared corresponding to both Pt(II) (Pt $4f_{7/2}$ at 73.03 eV; Pt $4f_{5/2}$ at 76.30 eV) and Pt(IV) (Pt $4f_{7/2}$ at 74.71 eV; Pt $4f_{5/2}$ at 77.81 eV). These data further confirmed the existence of Pt(II) in the NCs. The corresponding HRTEM images of AuNi and Pt-AuNi on Vulcan carbon are displayed in Figure S6. Also, the high-angle annular dark-field scanning transmission electron microscopy (HAADF-STEM) images clearly showed the presence of ca. 0.5 nm AuNi (Figure 3C) and Pt-AuNi NCs (Figure 3D) on Vulcan carbon, which was not resolved earlier due to the lack of contrast without carbon. The inset showing the size distribution histogram indicated that the mean particle size of the NCs after Pt decoration is not altered appreciably. Further, the elemental maps of AuNi/C (Figure S7) confirmed the presence of Au, Ni, S, and C. After Pt grafting, Pt was also detected in the elemental maps of Pt-AuNi/C (Figure 3E). The energydispersive X-ray spectra (EDS) obtained from HR-TEM analysis were recorded for both AuNi/C and Pt-AuNi/C (Figure S8). The atomic fractions determined for the Pt-AuNi/ C were ca. 0.11 for Au, 0.10 for Pt, and 0.12 for Ni.

The half-cell HER studies were conducted for AuNi/C and Pt-AuNi/C, and the performance was compared with the standard Pt/C catalyst. The geometrical surface area normalized iR-corrected HER polarization curves showed that the Pt-AuNi/C outperformed the AuNi/C (Figure 4A). The enhancement can be attributed to the synergistic interactions among Au, Pt, and Ni ions. Also, the Pt incorporation induced significant modification in the electronic structure of the NCs, as evidenced by XPS. The observed binding energy shift for Au 4f after Pt(II) grafting indicates the change in electronic environment of Au. Furthermore, the steady-state limiting behavior is partially obscured in the presence of carbon, although a mild inflection signaling the limitation is noticed (Figure S9). At 5 mA cm⁻², the electroless Pt decoration into the AuNi/C resulted in an overpotential change from 365 mV to 189 mV vs RHE (Figure 4B). Additionally, the electrochemical cathodization of Pt-AuNi/C by applying a potential of -2.5 V vs ag/AgCl for 5 s resulted in a further decrease in overpotential to 99 mV (Figure S10).

However, the reactivity is comparatively lower than the conventional Pt/C catalyst, which showed an overpotential of 45 mV at 5 mA cm⁻². This can be attributed to the very low loading of Pt. To investigate the intrinsic performance of the electrocatalysts, we calculated the electrochemical surface area (ECSA; Figure S11) by measuring the double layer capacitance. The results showed that the ECSA increases from 0.110 to 0.163 cm² after incorporation of Pt into the NCs framework (Figure 4C). The ECSA-normalized HER polarization curves also displayed a similar trend in performance as AuNi/C < Pt-AuNi/C < Pt/C (Figure S12). The corresponding comparison of overpotentials at 5 mA cm⁻² are shown in the bar diagram, denoting a lowering of overpotential after Pt incorporation (Figure 4D). The roughness factors of the electrocatalysts were then measured from the ECSA values and compared (Figure S13). The Pt-AuNi/C exhibited higher roughness factor than AuNi/C. However, it is lower than that of Pt/C, which is attributed to the higher number of active Pt sites in Pt/C. The Tafel plots derived from the ECSAnormalized HER polarization curve showed the slopes of AuNi/C, Pt-AuNi/C, and Pt/C as 80.7, 63.45, and 32.70 mV dec⁻¹, respectively (Figure 4E). These Tafel slope values represent intrinsic reaction kinetics of the catalyst, where lower slopes indicate faster HER kinetics. The commercial Pt/C catalyst exhibited a lower Tafel slope closer to the reported values, emphasizing the Volmer-Tafel mechanism and validating the precision of the measurements. Upon Pt grafting onto AuNi/C, a reduction in Tafel slope from 80.7 to 63.45 mV dec⁻¹ was observed, indicating a faster reaction rate. It signifies the efficiency of modification in facilitating enhanced HER performance. For Au NCs and Pt-grafted Au NCs, the Volmer-Heyrovsky mechanism was attributed, and we suggest that a similar mechanism is operative in our NCs. By extrapolating the Tafel slopes to zero overpotential, exchange current densities were calculated (Figure S14A), where Pt-AuNi/C was showing a better value of 0.045 mA cm⁻² than that of AuNi/C (0.019 mA cm⁻²). The higher value of exchange current density implies better inherent electron transfer kinetics. These values were optimized with respect to the exchange current density of Pt/C (≈ 0.221 mA cm⁻²). The specific activity of the Pt-AuNi/C $(0.787 \text{ mA cm}^{-2})$ was

ACS Applied Energy Materials

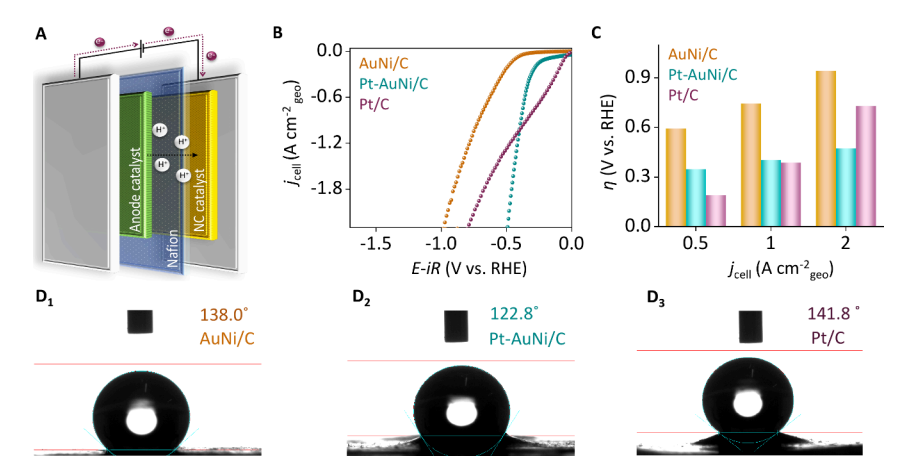


Figure 5. (A) Schematic showing the zero-gap cell configuration. (B) HER polarization curves as observed in the zero-gap cell and (C) corresponding bar diagram showing comparison of overpotentials. Contact angles measured with a water droplet on the PEM modified with (D_1) AuNi/C, (D_2) Pt-AuNi/C, and (D_3) Pt/C.

further obtained at 0.1 V that was ~3 times larger than that of the AuNi/C (0.243 mA cm⁻²; Figure S14B). To further investigate the enhanced HER activity, the charge transfer resistance of the systems was compared at an overpotential of -0.35 V vs Ag/AgCl using electrochemical impedance spectroscopy (EIS). The Nyquist plots with the corresponding Randles equivalent circuit are displayed in Figure 4F. Here, the Pt-AuNi/C showed a smaller semicircle with R_{ct} value of 10 $k\Omega$, appreciably lower than that of AuNi/C (200 $k\Omega).$ The lower R_{ct} for Pt-AuNi/C indicates faster interfacial charge transfer and better catalytic performance. It can be attributed to the change in electronic structure of the AuNi NCs after Pt grafting that facilitates electron transfer. The Nyquist plots for AuNi/C and Pt-AuNi/C at different overpotentials are displayed in Figure S15A and B, respectively, indicating reduced R_{ct} on increasing overpotential.

The long-term electrochemical stabilities of both AuNi/C and Pt-AuNi/C catalysts were then evaluated by chronopotentiometry at 10 mA cm⁻² of HER over 24 h (Figure S16A). To ensure consistent mass transport and remove the bubbles formed, the stability measurements were conducted using RDE at a constant speed of 900 rpm. Although overpotential increased initially, it got stabilized for the initial few hours followed by decrease in overpotential signaling the possible removal of impurities and consequent activation of the surface sites. The HER polarization curves of Pt-AuNi/C recorded before and after the stability test (Figure S16B) exhibited negligible shift in overpotential, highlighting the retention of catalytic performance over long-term run. Furthermore, postmortem surface analysis of the Pt-AuNi/C was conducted using XPS (Figure S17) that showed that Pt(II) was not reduced during the reaction. The retention of Pt in the +2 oxidation state indicates its stable incorporation within the NCs framework, minimizing the possibilities of leaching under electrochemical conditions and emphasizing the long-term stability of the system.

3.4. Performance of Pt-AuNi/C in Zero-Gap Cell. Since the reactivity of the Pt-AuNi/C is impressive for HER, we witnessed the mass-transport limitation that hampers the current density. High current density can be realized if a high concentration of protons is ensured at the surface of the NCs. In a practical sense, high proton concentration can be realized in a zero-gap cell, where high current density on Pt-AuNi/C

may be achieved. The schematic describing the zero-gap cell configuration is provided in Figure 5A. Hence, we recorded and compared the HER polarization curves from a zero-gap cell at 25 °C, using 10% AuNi/C, 10% Pt-AuNi/C, and 10% Pt/C as cathode catalyst in the membrane electrode assembly with IrO₂ as anode catalyst (Figure 5B). At low current densities, Pt/C exhibited better performance; however, at moderate current densities, both Pt/C and Pt-AuNi/C exhibited similar efficacies. Interestingly, at higher current densities, Pt-AuNi/C exhibited an extraordinary performance with the overpotential of 0.5 V at 2.3 A cm⁻², which is 0.3 V lower in comparison to Pt/C (Figure 5C). This observation highlights the suitability of precision NC-based HER electrocatalysts as they achieve the benchmark current density for commercial applications (>2 mA cm⁻²). Notably, only 0.55 mg cm⁻² Pt-AuNi/C or 55 µg cm⁻² ligand-protected NCs were used during cell fabrication, indicating exceptionally low catalyst loading. Out of this 55 μ g cm⁻², the atomic fractions of active metals were very low, as evidenced in the EDS analysis. This result demonstrates that the intrinsic reactivity of the NCs is higher, and the enhanced supply of protons assured higher current density. The contact angle measurements further proved the versatility of the material, as evidenced by the comparatively lower contact angle (122.8°) of the Pt-AuNi/C coated membrane, indicating the better wettability of the electrocatalyst and improved bubble removal kinetics that would reduce the activation/concentration overpotentials (Figure 5E). 48-51 Lower contact angle and improved bubble removal kinetics of Pt-AuNi/C are in good agreement with the observed better performance of the same at higher current densities. Whereas for Pt/C, higher bubble coverage due to the vigorous reaction would block the active sites.

Besides, facile bubble removal from the NCs could be linked to the modified hydrogen evolution mechanism. ^{37,38} Specifically, this modified Volmer–Heyrovsky mechanism involves the formation of adsorbed molecular hydrogen on the catalyst surface, which subsequently undergoes slow desorption and acts as a rate-determining step in Au NCs. This pathway facilitates the formation of smaller hydrogen bubbles that detach from the surface sites easily. The facile removal of bubbles prevents the growth of larger bubbles and ensures the continuous exposure of the active sites to obtain stable and efficient performance.

4. CONCLUSIONS

In conclusion, the carbon-supported Pt-AuNi NC electrocatalyst exhibited a more enhanced reactivity of the hydrogen evolution reaction (HER) than that of AuNi NCs. The origin of the enhanced reactivity might stem from the possible confinement of the diffusion field at the level of NCs as witnessed in the unusual quasi steady-state limiting behavior of current-potential characteristics. This was interpreted as an effect of a random array-like arrangement of NCs. The transition from quasi-steady-state limiting behavior to masstransport effect free current-potential characteristics explains the overlap of diffusion fields at t > 0 due to randomness of the NCs arrangements. The catalyst was also tested in a zero-gap cell to assess the hydrogen evolution characteristics of the Pt-AuNi NCs. The lower HER overpotential measured on Pt-AuNi/C than that of Pt/C at ca. 2 A cm⁻² in a zero-gap cell highlights the suitability of NCs for practical application to generate green hydrogen.

ASSOCIATED CONTENT

Supporting Information

The Supporting Information is available free of charge at https://pubs.acs.org/doi/10.1021/acsaem.5c01771.

Scheme for synthesis and purification of AuNi NCs; XPS spectra of NCs; CV of NCs before and after Pt grafting; CO-stripping CV of Pt-AuNi; HER polarization curves of Pt-AuNi/C at different rotation rates; HR-TEM images of AuNi/C and Pt-AuNi/C; HAADF-STEM and elemental maps of AuNi/C; EDS spectra of AuNi/C and Pt-AuNi/C; enlarged low-potential region of HER polarization curve; HER polarization curves after electrochemical activation; ECSA calculation; ECSA-normalized HER polarization curve; comparison of roughness factor; exchange current density calculation; specific capacitance calculation; Nyquist plots of AuNi/C and AuNi-Pt/C at different overpotentials; stability test of Pt-AuNi/C and AuNi/C for 24 h; and XPS spectra of Pt-AuNi/C after the stability test.(PDF)

AUTHOR INFORMATION

Corresponding Author

Jeyabharathi Chinnaiah — Electroplating and Electrometallurgy Division, CSIR-Council of Scientific and Industrial Research, Karaikudi, Tamil Nadu 630003, India; Academy of Scientific and Innovative Research (AcSIR), Ghaziabad 201002, India; orcid.org/0000-0002-4098-007X; Email: cjeyabharathi@cecri.res.in

Authors

Lakshmi Kavalloor Murali — Electroplating and Electrometallurgy Division, CSIR-Council of Scientific and Industrial Research, Karaikudi, Tamil Nadu 630003, India; Academy of Scientific and Innovative Research (AcSIR), Ghaziabad 201002, India; orcid.org/0000-0001-5372-2726

Kayalvizhi Anandhan — Electrochemical Process Engineering Division, CSIR-Council of Scientific and Industrial Research, Karaikudi, Tamil Nadu 630003, India; Academy of Scientific and Innovative Research (AcSIR), Ghaziabad 201002, India Subbiah Ravichandran — Electrochemical Process Engineering Division, CSIR-Council of Scientific and Industrial Research, Karaikudi, Tamil Nadu 630003, India; orcid.org/0000-0002-9743-300X

Edakkattuparambil Sidharth Shibu — Smart Materials Lab, Department of Nanoscience and Technology (DNST), University of Calicut (UOC), Malappuram, Kerala 673635, India; © orcid.org/0000-0003-3057-4198

Complete contact information is available at: https://pubs.acs.org/10.1021/acsaem.5c01771

Author Contributions

The project was designed and supervised by J.C. The nanoclusters were synthesized and characterized by L.K.M. The electrochemical experiments were performed by L.K.M., and zero-gap cell experiments were conducted by K.A. The manuscript was drafted by L.K.M. and J.C. The manuscript was written through the contributions of E.S.S., S.R., and K.A. All authors have given approval for the final version of the manuscript.

Notes

The authors declare no competing financial interest.

ACKNOWLEDGMENTS

L.K.M. thanks the University Grants Commission (UGC), India, for the Senior Research Fellowship through the National Eligibility Test. J.C. thanks the Department of Science & Technology for funding through the SHRI scheme (DST/TDT/SHRI-42/2021). K.A., J.C., and S.R. thank the CSIR Mission mode project (HCP-44M1). E.S.S. thanks the Department of Science and Technology (DST) for the Promotion of University Research and Scientific Excellence grant (PURSE; SR/PURSE/2023/191). The authors thank the Central Instrumentation Facility (CIF), CSIR-CECRI, for Instrumentation support. Dr. Mymoona Paloli, Mr. Sainul Abid, and Mr. Subramani E. are acknowledged for their characterization support. CSIR-CECRI Ethics and Scientific Vigilance Committee Reference Number: CECRI/PESVC/Pubs./2025-033.

REFERENCES

- (1) Palmer, G. Renewables Rise above Fossil Fuels. *Nat. Energy* **2019**, *4*, 538–539.
- (2) Dresselhaus, M. S.; Thomas, I. L. Nature 2001, 414, 332-337.
- (3) Jacobson, M. Z.; Colella, W. G.; Golden, D. M. Atmospheric Science: Cleaning the Air and Improving Health with Hydrogen Fuel-Cell Vehicles. *Science* **2005**, *308*, 1901–1905.
- (4) Karim, S.; Tanwar, N.; Das, S.; Ranjit, R.; Banerjee, A.; Gulafshan, N.; Gupta, A.; Kumar, A.; Dutta, A. Shaping the Future of Green Hydrogen Production: Overcoming Conventional Challenges with Molecular Catalysts, Immobilization, and Scalable Electrolyzers. *ACS Catal.* **2025**, *15*, 1073–1096.
- (5) Turner, J. A. Sustainable Hydrogen Production. Science 2004, 305, 972-974.
- (6) Odenweller, A.; Ueckerdt, F. The Green Hydrogen Ambition and Implementation Gap. *Nat. Energy* **2025**, *10*, 110–123.
- (7) Grigoriev, S. A.; Porembsky, V. I.; Fateev, V. N. Pure Hydrogen Production by PEM Electrolysis for Hydrogen Energy. *Int. J. Hydrogen Energy* **2006**, *31*, 171–175.
- (8) Liu, R. T.; Xu, Z. L.; Li, F. M.; Chen, F. Y.; Yu, J. Y.; Yan, Y.; Chen, Y.; Xia, B. Y. Recent Advances in Proton Exchange Membrane Water Electrolysis. *Chem. Soc. Rev.* **2023**, *52*, 5652–5683.
- (9) Carmo, M.; Fritz, D. L.; Mergel, J.; Stolten, D. A Comprehensive Review on PEM Water Electrolysis. *Int. J. Hydrogen Energy* **2013**, 38, 4901–4934.

- (10) Kibsgaard, J.; Chorkendorff, I. Considerations for the Scaling-up of Water Splitting Catalysts. *Nat. Energy* **2019**, *4*, 430–433.
- (11) Ayers, K. E.; Renner, J. N.; Danilovic, N.; Wang, J. X.; Zhang, Y.; Maric, R.; Yu, H. Pathways to Ultra-Low Platinum Group Metal Catalyst Loading in Proton Exchange Membrane Electrolyzers. *Catal. Today* **2016**, *262*, 121–132.
- (12) Wen, Y.; Chen, P.; Wang, L.; Li, S.; Wang, Z.; Abed, J.; Mao, X.; Min, Y.; Dinh, C. T.; Luna, P. De; Huang, R.; Zhang, L.; Wang, L.; Wang, L.; Nielsen, R. J.; Li, H.; Zhuang, T.; Ke, C.; Voznyy, O.; Hu, Y.; Li, Y.; Goddard, W. A.; Zhang, B.; Peng, H.; Sargent, E. H. Stabilizing Highly Active Ru Sites by Suppressing Lattice Oxygen Participation in Acidic Water Oxidation. *J. Am. Chem. Soc.* **2021**, *143*, 6482–6490.
- (13) Minke, C.; Suermann, M.; Bensmann, B.; Hanke-Rauschenbach, R. Is Iridium Demand a Potential Bottleneck in the Realization of Large-Scale PEM Water Electrolysis? *Int. J. Hydrogen Energy* **2021**, *46*, 23581–23590.
- (14) Cherevko, S.; Geiger, S.; Kasian, O.; Kulyk, N.; Grote, J. P.; Savan, A.; Shrestha, B. R.; Merzlikin, S.; Breitbach, B.; Ludwig, A.; Mayrhofer, K. J. J. Oxygen and Hydrogen Evolution Reactions on Ru, RuO₂, Ir, and IrO₂ Thin Film Electrodes in Acidic and Alkaline Electrolytes: A Comparative Study on Activity and Stability. *Catal. Today* **2016**, 262, 170–180.
- (15) Zhang, Z.; Baudy, A.; Testino, A.; Gubler, L. Cathode Catalyst Layer Design in PEM Water Electrolysis toward Reduced Pt Loading and Hydrogen Crossover. ACS Appl. Mater. Interfaces 2024, 16, 23265–23277.
- (16) Du, Y.; Sheng, H.; Astruc, D.; Zhu, M. Atomically Precise Noble Metal Nanoclusters as Efficient Catalysts: A Bridge between Structure and Properties. *Chem. Rev.* **2020**, *120*, 526–622.
- (17) Yamazoe, S.; Koyasu, K.; Tsukuda, T. Nonscalable Oxidation Catalysis of Gold Clusters. *Acc. Chem. Res.* **2014**, *47*, 816–824.
- (18) Chakraborty, I.; Pradeep, T. Atomically Precise Clusters of Noble Metals: Emerging Link between Atoms and Nanoparticles. *Chem. Rev.* **2017**, *117*, 8208–8271.
- (19) Häkkinen, H. Atomic and Electronic Structure of Gold Clusters: Understanding Flakes, Cages and Superatoms from Simple Concepts. *Chem. Soc. Rev.* **2008**, *37*, 1847–1859.
- (20) Lakshmi, K. M.; Rival, J. V.; Sreeraj, P.; Nambiar, S. R.; Jeyabharathi, C.; Nonappa; Shibu, E. S. Precision Nanocluster-Based Toroidal and Supertoroidal Frameworks Using Photocycloaddition-Assisted Dynamic Covalent Chemistry. *Small* **2023**, *19*, 2207119.
- (21) Mu, C.; Liu, Z.; Yao, Q.; He, Q.; Xie, J. Engineering Metal Nanoclusters at the Atomic Level for Effective Electrocatalysis. *SmartMat* **2025**, *6*, No. e1317.
- (22) Sumner, L.; Sakthivel, N. A.; Schrock, H.; Artyushkova, K.; Dass, A.; Chakraborty, S. Electrocatalytic Oxygen Reduction Activities of Thiol-Protected Nanomolecules Ranging in Size from Au₂₈(SR)₂₀ to Au₂₇₉(SR)₈₄. *J. Phys. Chem. C* **2018**, *122*, 24809–24817.
- (23) Li, S.; Alfonso, D.; Nagarajan, A. V.; House, S. D.; Yang, J. C.; Kauffman, D. R.; Mpourmpakis, G.; Jin, R. Monopalladium Substitution in Gold Nanoclusters Enhances CO₂ Electroreduction Activity and Selectivity. ACS Catal. 2020, 10, 12011–12016.
- (24) Wang, J.; Xu, F.; Wang, Z. Y.; Zang, S. Q.; Mak, T. C. W. Ligand-Shell Engineering of a Au₂₈ Nanocluster Boosts Electrocatalytic CO₂ Reduction. *Angew. Chemie Int. Ed.* **2022**, *61*, 1–6.
- (25) Zhao, S.; Jin, R.; Abroshan, H.; Zeng, C.; Zhang, H.; House, S. D.; Gottlieb, E.; Kim, H. J.; Yang, J. C.; Jin, R. Gold Nanoclusters Promote Electrocatalytic Water Oxidation at the Nanocluster/CoSe₂ Interface. J. Am. Chem. Soc. **2017**, 139, 1077–1080.
- (26) Jin, T.; Shen, S.; Xu, A.; Pan, J.; Zhou, G.; Zhong, W. Triggering Intrinsic Electrochemical Hydrogen Evolution Activity within Heusler Alloys via Electronegativity-Induced Charge Rearrangement. *Small* **2025**, *21*, 2500667.
- (27) Yan, Z.; Liu, Z.; Zhou, G.; Jin, T.; Zhang, H.; Gu, L.; Gao, T.; Shen, S.; Zhong, W. Short-Path Hydrogen Spillover on CeO₂-Supported PtPd Nanoclusters for Efficient Hydrogen Evolution in Acidic Media. *Angew. Chemie Int. Ed.* **2025**, *64*, No. e202501964.

- (28) Qian, H.; Jiang, D. E.; Li, G.; Gayathri, C.; Das, A.; Gil, R. R.; Jin, R. Monoplatinum Doping of Gold Nanoclusters and Catalytic Application. *J. Am. Chem. Soc.* **2012**, *134*, 16159–16162.
- (29) Kwak, K.; Choi, W.; Tang, Q.; Kim, M.; Lee, Y.; Jiang, D. E.; Lee, D. A Molecule-like $PtAu_{24}(SC_6H_{13})_{18}$ Nanocluster as an Electrocatalyst for Hydrogen Production. *Nat. Commun.* **2017**, *8*, 14723.
- (30) Greeley, J.; Stephens, I. E. L.; Bondarenko, A. S.; Johansson, T. P.; Hansen, H. A.; Jaramillo, T. F.; Rossmeisl, J.; Chorkendorff, I.; Nørskov, J. K. Alloys of Platinum and Early Transition Metals as Oxygen Reduction Electrocatalysts. *Nat. Chem.* **2009**, *1*, 552–556.
- (31) Min, M. K.; Cho, J.; Cho, K.; Kim, H. Particle Size and Alloying Effects of Pt-Based Alloy Catalysts for Fuel Cell Applications. *Electrochim. Acta* **2000**, 45, 4211–4217.
- (32) Stamenkovic, V. R.; Fowler, B.; Mun, B. S.; Wang, G.; Ross, P. N.; Lucas, C. A.; Markovic, N. M. Improved Oxygen Reduction Activity on Pt₃Ni(111) via Increased Surface Site Availability. *Science* **2007**, *315*, 493–497.
- (33) Strasser, P.; Koh, S.; Anniyev, T.; Greeley, J.; More, K.; Yu, C.; Liu, Z.; Kaya, S.; Nordlund, D.; Ogasawara, H.; Toney, M. F.; Nilsson, A. Lattice-Strain Control of the Activity in Dealloyed Core-Shell Fuel Cell Catalysts. *Nat. Chem.* **2010**, *2*, 454–460.
- (34) Seong, H.; Jo, Y.; Efremov, V.; Kim, Y.; Park, S.; Han, S. M.; Chang, K.; Park, J.; Choi, W.; Kim, W.; Choi, C. H.; Yoo, J. S.; Lee, D. Transplanting Gold Active Sites into Non-Precious-Metal Nanoclusters for Efficient CO₂-to-CO Electroreduction. *J. Am. Chem. Soc.* **2023**, *145*, 2152–2160.
- (35) Zhu, M.; Wang, P.; Yan, N.; Chai, X.; He, L.; Zhao, Y.; Xia, N.; Yao, C.; Li, J.; Deng, H.; Zhu, Y.; Pei, Y.; Wu, Z. The Fourth Alloying Mode by Way of Anti-Galvanic Reaction. *Angew. Chemie Int. Ed.* **2018**, *57*, 4500–4504.
- (36) Gan, Z.; Xia, N.; Wu, Z. Discovery, Mechanism, and Application of Antigalvanic Reaction. *Acc. Chem. Res.* **2018**, *51*, 2774–2783.
- (37) Mymoona, P.; Rival, J. V.; Nonappa; Shibu, E. S.; Jeyabharathi, C. Platinum-Grafted Twenty-Five Atom Gold Nanoclusters for Robust Hydrogen Evolution. *Small* **2024**, *20*, 2308610.
- (38) Brust, M.; Gordillo, G. J. Electrocatalytic Hydrogen Redox Chemistry on Gold Nanoparticles. *J. Am. Chem. Soc.* **2012**, *134*, 3318–3321.
- (39) Grozovski, V.; Vesztergom, S.; Láng, G. G.; Broekmann, P. Electrochemical Hydrogen Evolution: H⁺ or H₂O Reduction? A Rotating Disk Electrode Study. *J. Electrochem. Soc.* **2017**, *164*, E3171–E3178.
- (40) Liu, X.; Koper, M. T. M. Electrochimica Acta The Effect of Weak Proton Donors on the Steady-State Behavior of Hydrogen Evolution in Mildly Acidic Media. *Electrochim. Acta* **2024**, *507*, 145068
- (41) Belding, S. R.; Compton, R. G. Transient Voltammetry at Electrodes Modified with a Random Array of Spherical Nanoparticles: Theory. *J. Phys. Chem. C* **2010**, *114*, 8309–8319.
- (42) Davies, T. J.; Compton, R. G. The Cyclic and Linear Sweep Voltammetry of Regular and Random Arrays of Microdisc Electrodes: Theory. *J. Electroanal. Chem.* **2005**, *585*, 63–82.
- (43) Montero, M. A.; Gennero De Chialvo, M. R.; Chialvo, A. C. Rotating Nanoparticle Array Electrode for the Kinetic Study of Reactions under Mixed Control. *Electrochim. Acta* **2010**, *56*, 756–761.
- (44) Oleinick, A.; Sliusarenko, O.; Svir, I.; Amatore, C. Editors' Choice—Review—Nanostructured Electrodes as Random Arrays of Active Sites: Modeling and Theoretical Characterization. *J. Electrochem. Soc.* **2020**, *167*, No. 013530.
- (45) Tomčík, P. Microelectrode Arrays with Overlapped Diffusion Layers as Electroanalytical Detectors: Theory and Basic Applications. *Sensors* **2013**, *13*, 13659–13684.
- (46) Bain, C. D.; Whitesides, G. M. Correlations between Wettability and Structure in Monolayers of Alkanethiols Adsorbed on Gold. J. Am. Chem. Soc. 1988, 110, 3665–3666.

- (47) Lecoeur, J.; Andro, J.; Parsons, R. The Behaviour of Water at Stepped Surfaces of Single Crystal Gold Electrodes. *Surf. Sci.* **1982**, 114, 320–330.
- (48) Qian, X.; Kim, K.; Jung, S. Multiphase, Multidimensional Modeling of Proton Exchange Membrane Water Electrolyzer. *Energy Convers. Manag.* **2022**, 268, 116070.
- (49) Liu, W.; Wang, X.; Wang, F.; Du, K.; Zhang, Z.; Guo, Y.; Yin, H.; Wang, D. A Durable and pH-Universal Self-Standing MoC–Mo₂C Heterojunction Electrode for Efficient Hydrogen Evolution Reaction. *Nat. Commun.* **2021**, *12*, 1–10.
- (50) Ross, B.; Haussener, S.; Brinkert, K. Impact of Gas Bubble Evolution Dynamics on Electrochemical Reaction Overpotentials in Water Electrolyser Systems. *J. Phys. Chem. C* **2025**, *129*, 4383–4397.
- (51) Balaji, R.; Senthil, N.; Vasudevan, S.; Ravichandran, S.; Mohan, S.; Sozhan, G.; Madhu, S.; Kennedy, J.; Pushpavanam, S.; Pushpavanam, M. Development and Performance Evaluation of Proton Exchange Membrane (PEM) Based Hydrogen Generator for Portable Applications. *Int. J. Hydrogen Energy* **2011**, *36*, 1399–1403.

